SCIENCE CHINA
Technological Sciences

February 2011 Vol.54 No.2: 420–430
doi: 10.1007/s11431-010-4235-6

High-frequency interference in low strain integrity testing of large-diameter pipe piles

DING XuanMing[1*], LIU HanLong[2] & ZHANG Bo[3]

[1] *National Engineering Research Center of Water Resources Efficient Utilization and Engineering Safety, Hohai University, Nanjing 210098, China;*
[2] *Key Laboratory of Ministry of Education for Geomechanics and Embankment Engineering, Hohai University, Nanjing 210098, China;*
[3] *School of Civil and Environmental Engineering, Nanyang Technological University, 50 Nanyang Avenue 639798, Singapore*

Received June 3, 2010; accepted November 22, 2010

The high-frequency interference exists obviously in low strain integrity testing of large-diameter pipe pile when a transient point load is applied. An analytical solution of vertical vibratory response of large-diameter pipe piles in low strain testing is deduced in this paper. The analytical solution is verified by both numerical simulation and model test results. The time-domain velocity responses on pile top are analyzed. The calculation results indicate that the time-domain responses at various points suffer different high-frequency interferences, thus the peak values and phases of different points are different. The influence of vibratory modes on high-frequency interference is analyzed. It is found that the high-frequency interference at 90° point mainly derives from the second flexural mode, but for other points it mainly originates from the first flexural mode. The factors affecting the frequency and peak value of interference waves have been investigated in this study. The results indicate that the larger radius angle between the receiving and 90° points leads to greater peak value of high frequency wave crest. The least high-frequency interference is detected at the angle of 90°. The frequency of interference waves is decreased with the increase of pile radius, while the peak value is almost constant. The frequency is also related to pile modulus, i.e. the larger pile modulus results in greater frequency. The peak value varies with impulse width and soil resistance, i.e., the wider impulse width and larger soil resistance cause smaller peak value. In conclusion, the frequency of interference waves is dependent on the geometrical and mechanics characteristics of the piles such as pile radius and modulus, but independent of the external conditions such as impulse width and soil resistance. On the other hand, the peak value of interference waves is mainly dependent on the external conditions but independent of the geometrical and mechanics characteristics of the piles. In practice, some external measures should be adopted to weaken high-frequency interference such as using soft hammer, hammer cushion and adopting suitable receiving point.

large-diameter pipe pile, low strain integrity testing, high-frequency interference, vibratory response, analytic solution

Citation: Ding X M, Liu H L, Zhang B. High-frequency interference in low strain integrity testing of large-diameter pipe piles. Sci China Tech Sci, 2011, 54: 420–430, doi: 10.1007/s11431-010-4235-6

1 Introduction

A new type of pile called cast-in-situ concrete large-diameter pipe pile (referred as PCC pile) has been developed and widely applied in China for reinforcing soft ground due to its larger side frictional resistance and use of less concrete. The PCC piling technique mainly consists of driving an open-ended double walled steel casing by vibratory method, forming an annulus void, pouring concrete, and retrieving the steel casing [1–4]. The casting quality is of great importance for such kind of cast-in-situ pile. The common

*Corresponding author (email: dxmhhu@163.com)

method for pile quality inspection is static load testing or dynamic testing. A large amount of surcharge load is required in static load testing. Furthermore this method is costly and time-consuming. This test is usually conducted for limited piles which is representative for all the piles quality check. Low strain dynamic testing has been proved to be an effective method [5,6]. The problems regarding dynamic pile testing has attracted attentions of researchers for more than 50 years [7–13]. The methodology is based on one-dimensional (1D) wave theory, with this theory the wave propagation is assumed as plane-section and the pile is regarded as a 1D elastic pole, hence it is only applicable to small diameter pile. However, the cross section of PCC pile is a large-diameter hollow cylinder, the stress is non-axisymmetric when the pile head is subjected to transient point load during the low strain integrity testing. In fact, the wave propagation in pile shaft is a three-dimensional (3D) problem. There are obvious 3D effects and high-frequency interference in testing such kind of large diameter pipe pile. The high-frequency interference has not been taken into consideration in 1D wave theory, so a 3D wave theory applied to such kind of large diameter pile should be developed.

Previous studies have demonstrated that the velocity responses on pile top are influenced by high-frequency waves, which covered the reflected wave crests and made inaccurate judgment of integrity, so the study on high-frequency interference is of great importance for dynamic testing on large-diameter pipe pile [14]. The problem of high-frequency interference was studied by finite element method (FEM) [15,16]. The FEM results showed that the superposition of radial natural vibration modes resulted in high-frequency waves with various frequencies and peak values. For the time costing and complexity of numerical method, only a few numerical examples were presented by previous studies [16], so the frequency, peak value and influencing factors of high-frequency waves need to be studied further.

In this paper, the high-frequency interference is studied by an analytical formula. The effects of radius angle, pile radius and length, modulus, impulse width and soil resistance on high-frequency interference are investigated. The frequency and peak value of high-frequency waves are analyzed. The methods to weaken interference of high-frequency waves are proposed.

2 Analytical solution and its verification

2.1 Assumptions and computational model

The cylindrical coordinate system and the computational model are shown in Figure 1, where H represents pile length, h represents wall thickness, R_1 represents outer radius and R_2 represents inner radius. The assumptions are made as follows:

(1) The soil resistance is modeled by the Winkler model as shown in Figure 1, where the elastic and damping coefficients of outer soil are k_O and δ_O. For inner soil, the coefficients are k_I and δ_I . For pile-bottom soil, those are k_p and δ_p, respectively.

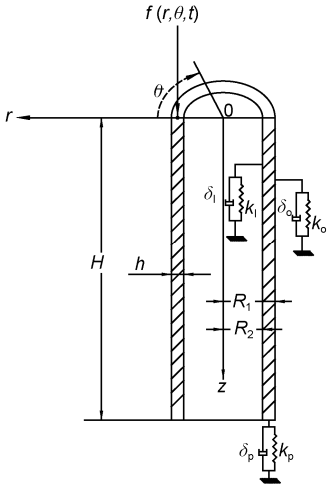

Figure 1 Computational model.

(2) The deformation of pile shaft is elastic and the damping of concrete is considered as viscous damping.

(3) The vibration of the pile-soil system is a small deformation problem.

(4) The applied force of exciting hammer is regarded as a transient point load, the coordinates of the action point are z=0, θ=0 and r=R_0, where R_0=0.5(R_1+R_2) is the average pile radius.

(5) The pipe pile in low strain testing is subjected to an impulse load. The exciting force $f(r,\theta, t)$ is simulated with semisinusoidal impulse as

$$f(r,\theta,t)=\begin{cases} Q\sin\left(\dfrac{2\pi}{T}t\right)\delta(r-R_0)\delta(\theta) & \left(t\leqslant\dfrac{T}{2}\right), \\ 0 & \left(t>\dfrac{T}{2}\right), \end{cases} \tag{1}$$

where T is the period, Q is the peak value, $\delta(\ )$ is a Dirac function.

2.2 Wave equation and boundary conditions

Considering the force balance in z direction and Newton's second law of motion, the following dynamic equilibrium equation can be established:

$$\frac{\partial\sigma_z}{\partial z}+\frac{1}{r}\frac{\partial\tau_{\theta z}}{\partial\theta}+\frac{\partial\tau_{rz}}{\partial r}+\frac{\tau_{rz}}{r}=\rho\frac{\partial^2 u}{\partial t^2}. \tag{2}$$

The constitutive relations of the concrete of pile shaft are

$$\begin{cases} \sigma_z=(\lambda+2G)\dfrac{\partial u}{\partial z}+\eta\dfrac{\partial^2 u}{\partial t\partial z}, \\ \tau_{\theta z}=\dfrac{G}{r}\dfrac{\partial u}{\partial\theta}+\dfrac{\eta}{r}\dfrac{\partial^2 u}{\partial t\partial\theta}, \\ \tau_{rz}=G\dfrac{\partial u}{\partial r}+\eta\dfrac{\partial^2 u}{\partial t\partial r}. \end{cases} \tag{3}$$

Substituting eq. (3) into eq. (2), the 3D wave equation under non-axisymmetric condition can be established as follows:

$$\begin{aligned}&(\lambda+2G)\frac{\partial^2 u(z,\theta,r,t)}{\partial z^2}+\eta\frac{\partial^3 u(z,\theta,r,t)}{\partial t\partial z^2}+\frac{G}{r^2}\frac{\partial^2 u(z,\theta,r,t)}{\partial \theta^2}\\&+\frac{\eta}{r^2}\frac{\partial^3 u(z,\theta,r,t)}{\partial t\partial \theta^2}+G\frac{\partial^2 u(z,\theta,r,t)}{\partial r^2}+\eta\frac{\partial^3 u(z,\theta,r,t)}{\partial t\partial r^2}\\&+\frac{G}{r}\frac{\partial u(z,\theta,r,t)}{\partial r}+\frac{\eta}{r}\frac{\partial^2 u(z,\theta,r,t)}{\partial t\partial r}=\rho\frac{\partial^2 u(z,\theta,r,t)}{\partial t^2},\end{aligned}\tag{4}$$

where η is the viscous damping coefficient of the pile shaft; $u(z,\theta,r,t)$ is the vertical displacement at time t; ρ is the density of the pile shaft; λ is the Lame constant and G is the shear modulus of the pile shaft, which can be calculated by Young's modulus E and Poisson's ratio ν by the following equations:

$$\lambda=\frac{E\nu}{(1+\nu)(1-2\nu)},\quad G=\frac{E}{2(1+\nu)}.$$

The vertical stress σ_z is equal to exciting impulse when z=0, thus the boundary condition on pile top can be written as

$$\left((\lambda+2G)\frac{\partial u}{\partial z}+\eta\frac{\partial^2 u}{\partial t\partial z}\right)\Big|_{z=0}=f(r,\theta,t).\tag{5}$$

The vertical stress σ_z is equal to reaction force of pile bottom soil when z=H, thus the boundary condition on pile bottom can be written as

$$\left((\lambda+2G)\frac{\partial u}{\partial z}+\eta\frac{\partial^2 u}{\partial t\partial z}+k_P u+\delta_P\frac{\partial u}{\partial t}\right)\Big|_{z=H}=0.\tag{6}$$

The shear stress τ_{rz} is equal to resistance of outer soil when r=R_1, thus the boundary condition on the outer side of the pile can be written as

$$\left(G\frac{\partial u}{\partial r}+\eta\frac{\partial^2 u}{\partial t\partial r}+k_{\mathrm{O}}u+\delta_{\mathrm{O}}\frac{\partial u}{\partial t}\right)\Big|_{r=R_1}=0.\tag{7}$$

The shear stress τ_{rz} is equal to resistance of inner soil when r=R_2, thus the boundary condition on the inner side of the pile can be written as

$$\left(G\frac{\partial u}{\partial r}+\eta\frac{\partial^2 u}{\partial t\partial r}-k_1 u-\delta_1\frac{\partial u}{\partial t}\right)\Big|_{r=R_2}=0.\tag{8}$$

Before low strain integrity testing, the pile is stationary, so the initial conditions can be written as

$$\begin{cases}u(z,\theta,r,t)\big|_{t=0}=0,\\ \dfrac{\partial u(z,\theta,r,t)}{\partial t}\Big|_{t=0}=0.\end{cases}\tag{9}$$

2.3 Solving process of the method

Combining the initial conditions eqs. (9), by performing Laplace transformation to eq.(4), we can obtain:

$$\begin{aligned}&(\lambda+2G+\eta s)\frac{\partial^2 U(z,\theta,r,s)}{\partial z^2}+\frac{G+\eta s}{r^2}\frac{\partial^2 U(z,\theta,r,s)}{\partial \theta^2}\\&+(G+\eta s)\frac{\partial^2 U(z,\theta,r,s)}{\partial r^2}+\frac{G+\eta s}{r}\frac{\partial U(z,\theta,r,s)}{\partial r}\\&=\rho s^2 U(z,\theta,r,s),\end{aligned}\tag{10}$$

where $U(z,\theta,r,s)$ is the Laplace transformation of $u(z,\theta,r,t)$. By separation of variables, $U(z,\theta,r,s)$ can be transformed into

$$U(z,\theta,r,s)=Z(z)\Phi(\theta)R(r).\tag{11}$$

By substituting eq. (11) into eq. (10), one obtains

$$\begin{aligned}&(\lambda+2G+\eta s)\frac{Z''(z)}{Z(z)}+\frac{G+\eta s}{r^2}\frac{\Phi''(\theta)}{\Phi(\theta)}\\&+(G+\eta s)\frac{R''(r)}{R(r)}+\frac{G+\eta s}{r}\frac{R'(r)}{R(r)}=\rho s^2.\end{aligned}\tag{12}$$

Given

$$\frac{\Phi''(\theta)}{\Phi(\theta)}=\kappa.\tag{13}$$

In a cylindrical coordinate system, $\Phi(\theta)$ is a periodic function with a period of 2π, as a result, only when κ=$-m^2$, the above qualification can be satisfied. Hence, the general solution is

$$\Phi_m(\theta)=C\cos(m\theta)+D\sin(m\theta),\tag{14}$$

where m=0, 1, 2,…, C and D are undetermined coefficients.

According to the mechanical characteristics, it is known that $U(z,\theta,r,s)$ should be a even function of θ, therefore, D=0 is obtained in eq.(14).

Hence,

$$\Phi_m(\theta)=C\cos(m\theta).\tag{15}$$

Given

$$\frac{R''(r)}{R(r)}+\frac{1}{r}\frac{R'(r)}{R(r)}-\frac{m^2}{r^2}=-\beta_m^2.\tag{16}$$

Eq. (16) is a Bessel equation, the solution of which is

$$R_m(r)=AJ_m(\beta_m r)+BY_m(\beta_m r),\tag{17}$$

where $J_m(\ )$ and $Y_m(\ )$ are the first and second kinds of Bessel function of order m, respectively. A and B are undetermined coefficients.

By performing Laplace transformation to eqs. (7) and (8), and then substituting eq. (17) into them, it yields

$$\begin{aligned}\frac{A}{B}&=-\frac{\beta_m Y_m'(\beta_m R_1)+\dfrac{k_{\mathrm{O}}+\delta_{\mathrm{O}}s}{G+\eta s}Y_m(\beta_m R_1)}{\beta_m J_m'(\beta_m R_1)+\dfrac{k_{\mathrm{O}}+\delta_{\mathrm{O}}s}{G+\eta s}J_m(\beta_m R_1)}\\&=\frac{-\beta_m Y_m'(\beta_m R_2)+\dfrac{k_1+\delta_1 s}{G+\eta s}Y_m(\beta_m R_2)}{\beta_m J_m'(\beta_m R_2)-\dfrac{k_1+\delta_1 s}{G+\eta s}J_m(\beta_m R_2)}.\end{aligned}\tag{18}$$

In eq. (18), only variable quantity β_m is unknown. For a number m, the n roots of eq. (18) can be easily solved by iteration process. Then $\beta_m=\beta_{m1}, \beta_{m2}, \ldots, \beta_{mn}$ are obtained.

Writing

$$\zeta_{mn}=-\frac{\beta_{mn}Y'_m(\beta_{mn}R_1)+\dfrac{k_O+\delta_O s}{G+\eta s}Y_m(\beta_{mn}R_1)}{\beta_{mn}J'_m(\beta_{mn}R_1)+\dfrac{k_O+\delta_O s}{G+\eta s}J_m(\beta_{mn}R_1)},$$

then,

$$R_{mn}(r)=B[\zeta_{mn}J_m(\beta_{mn}r)+Y_m(\beta_{mn}r)]. \tag{19}$$

Given

$$\frac{Z''(z)}{Z(z)}=\alpha_{mn}^2. \tag{20}$$

By substituting eqs. (13), (16) and (20) into eq. (12), one obtains

$$\alpha_{mn}=\sqrt{\frac{(G+\eta s)\beta_{mn}^2+\rho s^2}{(\lambda+2G+\eta s)}}. \tag{21}$$

The general solution of eq. (20) is

$$Z_{mn}(z)=C_{mn}e^{\alpha_{mn}z}+D_{mn}e^{-\alpha_{mn}z}, \tag{22}$$

where C_{mn} and D_{mn} are undetermined coefficients.

Combining eqs. (15), (19) and (22), the displacement of the pile shaft is

$$U_{mn}(z,\theta,r,s)=\begin{bmatrix}\zeta_{mn}J_m(\beta_{mn}r)+\\ Y_m(\beta_{mn}r)\end{bmatrix}\cos(m\theta)\begin{pmatrix}C_{mn}e^{\alpha_{mn}z}+\\ D_{mn}e^{-\alpha_{mn}z}\end{pmatrix}, \tag{23}$$

$$U(z,\theta,r,s)=\sum_{m=0}^{\infty}\sum_{n=1}^{\infty}U_{mn}(z,\theta,r,s). \tag{24}$$

Performing Laplace transformation to eq. (5), and then substituting eq. (24) into it, one obtains

$$\begin{pmatrix}\lambda+2G\\ +\eta s\end{pmatrix}\sum_{m=0}^{\infty}\sum_{n=1}^{\infty}\begin{bmatrix}\zeta_{mn}J_m(\beta_{mn}r)\\ +Y_m(\beta_{mn}r)\end{bmatrix}\cos(m\theta)\alpha_{mn}\begin{pmatrix}C_{mn}\\ -D_{mn}\end{pmatrix}$$
$$=F(s)\delta(\theta)\delta(r-R_0), \tag{25}$$

where $F(s)$ is the Laplace transform of the function $Q\sin\left(\frac{2\pi}{T}t\right)\left(0\leqslant t\leqslant\frac{T}{2}\right)$.

It is proved that the solutions of Bessel equation meet the following orthogonality:

$$\int_{R_2}^{R_1}rR_{mi}(r)R_{mj}(r)\mathrm{d}r=\begin{cases}0 & (i\neq j),\\ \int_{R_2}^{R_1}rR_{mi}^2(r)\mathrm{d}r & (i=j),\end{cases} \tag{26}$$

where,

$$R_{mi}(r)=\zeta_{mi}J_m(\beta_{mi}r)+Y_m(\beta_{mi}r),$$
$$R_{mj}(r)=\zeta_{mj}J_m(\beta_{mj}r)+Y_m(\beta_{mj}r).$$

Based on the orthogonality of $\cos(m\theta)$ and Bessel function $R_{mn}(r)$, two sides of eq. (25) are multiplied by $\cos(m\theta)$ and $R_{mn}(r)$, and then integrating on interval $[R_2,R_1]$, it is obtained that

$$C_{mn}-D_{mn}=\xi_{mn}F(s), \tag{27}$$

where,

$$\xi_{mn}=\begin{cases}\dfrac{\left[\zeta_{mn}J_m(\beta_{mn}R_0)+Y_m(\beta_{mn}R_0)\right]R_0}{2\pi(\lambda+2G+\eta s)\alpha_{mn}\int_{R_2}^{R_1}r\left[\begin{matrix}\zeta_{mn}J_m(\beta_{mn}r)\\ +Y_m(\beta_{mn}r)\end{matrix}\right]^2\mathrm{d}r} & (m=0),\\ \dfrac{\left[\zeta_{nm}J_m(\beta_{mn}R_0)+Y_m(\beta_{mn}R_0)\right]R_0}{\pi(\lambda+2G+\eta s)\alpha_{mn}\int_{R_2}^{R_1}r\left[\begin{matrix}\zeta_{mn}J_m(\beta_{mn}r)\\ +Y_m(\beta_{mn}r)\end{matrix}\right]^2\mathrm{d}r} & (m\neq 0).\end{cases}$$

By performing Laplace transformation to eq. (6), and then substituting eq. (24) into it, one obtains

$$C_{mn}=\chi_{mn}D_{mn}, \tag{28}$$

where,

$$\chi_{mn}=\frac{(\lambda+2G+\eta s)\alpha_{mn}-(k_p+\delta_p s)}{(\lambda+2G+\eta s)\alpha_{mn}+(k_p+\delta_p s)}e^{-2\alpha_{mn}H}.$$

By eqs.(27) and (28), one obtains

$$\begin{cases}C_{mn}=\dfrac{\chi_{mn}\xi_{mn}}{\chi_{mn}-1}F(s),\\ D_{mn}=\dfrac{\xi_{mn}}{\chi_{mn}-1}F(s).\end{cases} \tag{29}$$

Substituting eqs. (29) to eq. (23), the analytical solution is obtained:

$$U_{mn}(z,\theta,r,s)=\left[\zeta_{mn}J_m(\beta_{mn}r)+Y_m(\beta_{mn}r)\right]\cos(m\theta)$$
$$\cdot\left(\chi_{mn}e^{\alpha_{mn}z}+e^{-\alpha_{mn}z}\right)\frac{\xi_{mn}}{\chi_{mn}-1}F(s). \tag{30}$$

In eq. (30), m=0 represents the axisymmetric mode, which contains infinitely many modes: n=1, 2, 3,…, and m>0 represents the non-axisymmetric mode, which also contains infinitely many modes: n=1, 2, 3,….

If given $s=i\omega$ in eq. (30), the Laplace transformation is equivalent to one-sided Fourier transformation, then the frequency domain response is obtained as $U(z,\theta, r, i\omega)$.

The velocity response is obtained as

$$V_{mn}(z,\theta,r,i\omega)=\left[\zeta_{mn}J_m(\beta_{mn}r)+Y_m(\beta_{mn}r)\right]\cos(m\theta)$$
$$\cdot\left(\chi_{mn}e^{\alpha_{mn}z}+e^{-\alpha_{mn}z}\right)\frac{i\omega\xi_{mn}}{\chi_{mn}-1}F(i\omega), \tag{31}$$

$$V(z,\theta,r,i\omega)=\sum_{m=0}^{\infty}\sum_{n=1}^{\infty}V_{mn}(z,\theta,r,i\omega). \tag{32}$$

The time domain responses are obtained by Inverse Fou-

rier Transformation as

$$u_{mn}(z,\theta,r,t) = IFT[U_{mn}(z,\theta,r,i\omega)] = \frac{1}{2\pi}\int_{-\infty}^{+\infty} U_{mn}(z,\theta,r,i\omega)e^{i\omega t}\mathrm{d}\omega, \quad (33)$$

$$u(z,\theta,r,t) = \sum_{m=0}^{\infty}\sum_{n=1}^{\infty} u_{mn}(z,\theta,r,t), \quad (34)$$

$$v_{mn}(z,\theta,r,t) = IFT[V_{mn}(z,\theta,r,i\omega)] = \frac{1}{2\pi}\int_{-\infty}^{+\infty} V_{mn}(z,\theta,r,i\omega)e^{i\omega t}\mathrm{d}\omega, \quad (35)$$

$$v(z,\theta,r,t) = \sum_{m=0}^{\infty}\sum_{n=1}^{\infty} v_{mn}(z,\theta,r,t), \quad (36)$$

where ω is angular frequency with unit of rad/s, which can transform to frequency by $f=\omega/2\pi$; $u(z, \theta, r, t)$ is the displacement response of the pile shaft in time domain; $v(z, \theta, r, t)$ is the velocity response of the pile shaft in time domain.

2.4 Verification of analytical method

The 1D wave theory, 3D FEM and model tests are employed to verify the validity of analytical solution. Firstly, the 3D analytical method is compared with 1D wave theory. The parameters are shown in Table 1.

The stress waves in 3D model propagate in vertical, radial and circumferential directions, which reflect back from pile bottom, inner side and outer side and then superimpose each other, resulting in different dynamic responses among different points on pile head, namely 3D effects. Figure 2 shows that the peak value and arrival time of incident wave crests are different between 3D analytical solution and 1D wave theory because of the 3D effects. The high-frequency interference is obvious on velocity time history of 3D analytical solution but it is invisible in 1D wave theory. As the propagation of waves, the 3D effects are gradually weakened, so the reflected wave crests are almost the same.

The 1D wave theory based on plane-section assumption cannot reflect the real propagation of stress waves in low strain testing on large-diameter pipe piles, but the 3D analytical solution in this paper can predict 3D effects and high-frequency interference.

The 3D analytical method is also compared with FEM. In the FEM, the resistance of soil is also modeled by spring and damper as equivalent to the Winkler model, which are set along the outer, inner and bottom surfaces. A linear elastic FEM computer program is compiled with FORTRAN computer language.

The time difference between the incident and reflected wave crests is of great importance for low strain integrity testing. Figure 3 shows the time difference between the incident and reflected wave crests on pile top. The results of FEM and analytical solution are similar. The two curves in Figure 3 indicate that the larger the radius angle between the exciting point (θ = 0° or 360°) and the receiving point, the smaller the time difference; consequently, the shape of the curves is just like a sunken bowl, that is caused by the delay of the incident wave crest. The figure indicates that the results of analytical solution reach agreement with FEM results.

Table 2 shows the arrival time of the incident and reflected wave crests and their time differences. Compared with 1D wave theory, the arrival time of the incident wave crest is later at the points from 45° to 180°, and the arrival time of the reflected wave crest is also delayed. The time differences are larger than 1D wave theory at 0° and 45° points, but smaller at the other points. In low strain testing of a pipe pile, the receiver sensor is usually fixed at the 90° point, so the time at this point is used to detect pile length and depth of defect. There are time errors between 1D wave theory and 3D analytical solution at this point. For incident wave crest, the error is 0.47 ms; for the reflected wave crest,

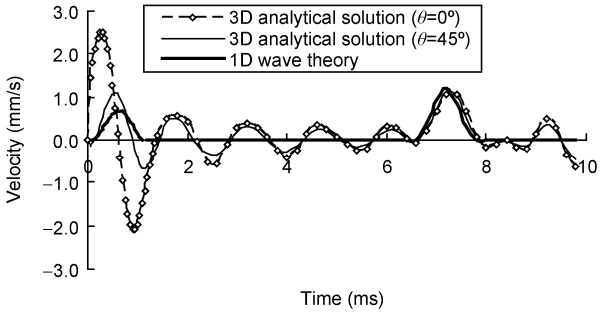

Figure 2 Comparison of the results of 1D wave theory and the analytical solution (z=0, r=0.44).

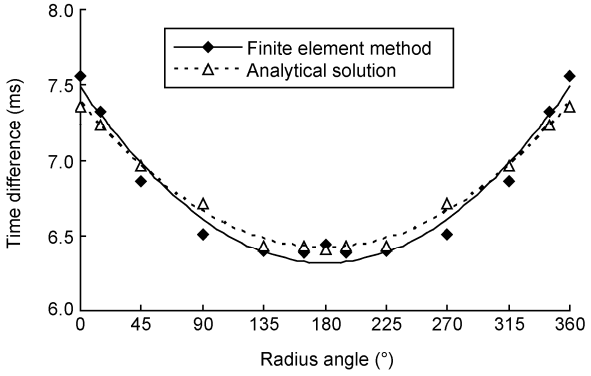

Figure 3 Comparison of time difference between incident and reflected wave crests (z=0, r=0.44).

Table 1 The parameters of pile and soil

E (GPa)	v	ρ (kg/m^3)	R_0 (m)	h (m)	H (m)	k_p (N/m^3)	δ_p (N s/m^3)	η (N s/m^2)	k_I,k_O (N/m^3)	δ_I,δ_O (N s/m^3)	Q (kN)	T (ms)
20	0.17	2400	0.44	0.12	10	10^5	10^4	0.1	10^2	10	1	2

Table 2 Arrival time of incident and reflected wave crests and their time differences (ms)

Theory	3D analytical solution					1D wave theory
	0°	45°	90°	135°	180°	
Incident wave	0.43	0.72	0.97	1.26	1.29	0.50
Reflected wave	7.69	7.68	7.68	7.69	7.70	7.43
Time difference	7.26	6.96	6.71	6.43	6.41	6.93

it is 0.25 ms; for time difference, it is 0.22 ms.

The analytical solution is further verified by model test results. A model PCC pile test was conducted in a large test chamber at Hohai University in Nanjing, China [17]. The size of the chamber is 5 m (length) ×4 m (width) ×7 m (height). The diameter of the PCC pile is 1.0 m with a wall thickness of 0.12 m and a pile length of 6.0 m. The Young's modulus of shaft concrete is 24 GPa. The applied impulse period is 4 ms. The characters of the physical mechanical parameters of the soil were obtained by laboratory tests [17]. Details of the test setup and testing procedures can be found in ref. [17]. Figures 4 and 5 present the comparison of test results and analytical solution. The figures indicate that the numerical results of analytical solution can well match the results of tests, thus the analytical solution is reasonable and reliable.

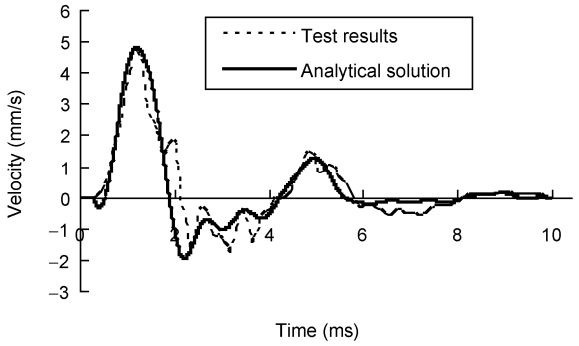

Figure 4 Comparison of velocity responses of analytical solution and model test result (z=0, θ=90, r=0.44).

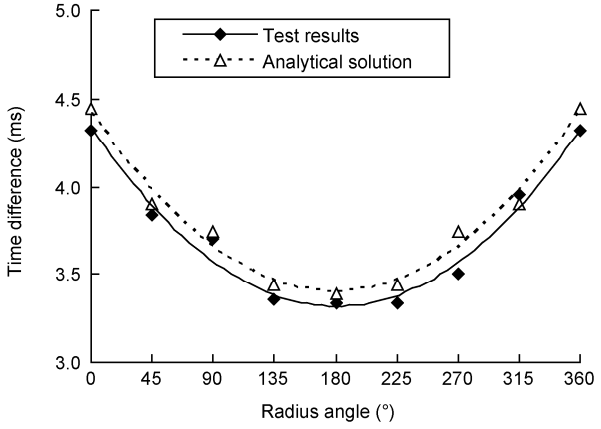

Figure 5 Time difference between incident and reflected wave crests of analytical solution and model test (z=0, r=0.44).

3 Source contributions of high-frequency waves

The load applied on top of PCC pile in low strain testing is non-axisymmetrical, so the dynamic responses are closely related to the position of measuring points, and the velocity responses are various among measuring points with different radius angles.

The velocity responses time history at 0°, 45°, 90°, 135° and 180° points are shown in Figure 6. The input parameters are the same as shown in Table 1.

Because of the interference of high-frequency waves, the velocity response curves are not steady between the incident and reflected wave crests. As a result, many high frequency oscillatory wave crests are formed before the reflected waves from the pile bottom arrive. The peak values and phases of high-frequency interference are not the same at different points. The wave crests and hollows of high-frequency interference waves are formed at almost the same time. For instance, the time of wave crests at the 0° and 45° points is the same as that of the wave hollows at the 135° and 180° points. Whereas, the time of wave crests at the 135° and 180° points is the same as that of the wave hollows at the 0° and 45° points, so the phase difference is just 180°. The velocity response curve is the steadiest at the angle of 90°, which indicates that the point at the angle of 90° suffers the least high-frequency interference, thus the radius angles between exciting hammer and receiving accelerometer should be set apart at approximately 90° in engineering application. The results also indicate that the larger the radius angle between the receiving point and 90° point, the greater the peak value of high frequency wave crest.

The above characteristics of high-frequency interference can be explained by vibratory modes. The time-domain velocity responses of various modes are calculated by eq. (31). The fundamental modes (m=0) are axisymmetric, so the dynamic responses among different points in circumferential direction are the same. It can be seen from Figure 7 that the peak values of the incident and reflected waves of mode v_{01} (m=0, n=1) are the largest, and the peak values of the other modes (m=0, n>1) are far less than v_{01}. There are few

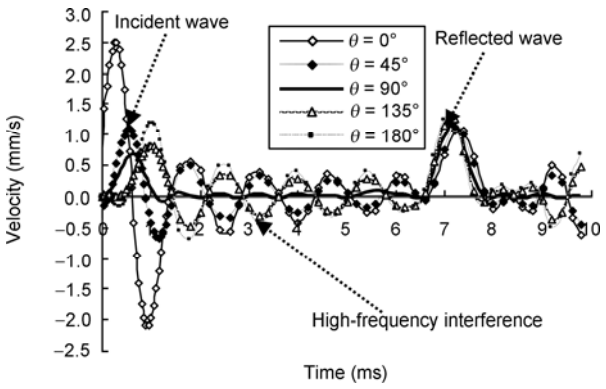

Figure 6 Velocity responses on top of intact pile at different points along circumferential direction (z=0, r=0.44).

high-frequency waves between the incident and reflected waves, so the axisymmetric modes are not the source of high-frequency interference. It can be seen from Figure 8 that the input force excites the first flexural mode v_{11} (m=1, n=1) of the pipe pile. The high-frequency interference is visible at the points with θ=0°, 45°, 135° and 180°. But since the velocity in the first flexural mode varies with cos(θ), there is little high-frequency interference at the point with θ=90°. The high-frequency interference at θ=90° mainly comes from the second flexural mode (m=2) where cos(2θ) is non-zero (as shown in Figure 9), however, the peak value of high-frequency waves of v_{21} is very small, so the point with θ=90° suffers the least high-frequency interference.

The velocity response of the first flexural mode v_{11} is comparatively large except the 90° point. The peak value of the high-frequency interference of mode v_{11} is far greater than the modes when n>1(shown as Figures 10 and 11), and it even exceeds the incident waves, which indicates that the first flexural mode v_{11} is the main source contributions of high-frequency waves.

Because the value of cos(θ) when θ=0° or 45° is positive but when θ=135° or 180° it is negative, the phases of high-frequency waves at the points with θ=0° or 45° are phase reversal compared with those at the points with θ=135° or 180°. Similarly, the absolute value of cos(θ) when θ=0° or 180° is 1 but when θ=45° or 135° it is about 0.707, as a result, the peak value of high-frequency waves at the points

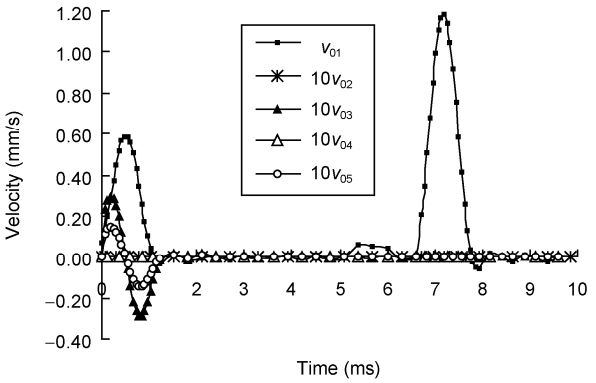

Figure 7 Comparison of velocity responses of axisymmetric modes.

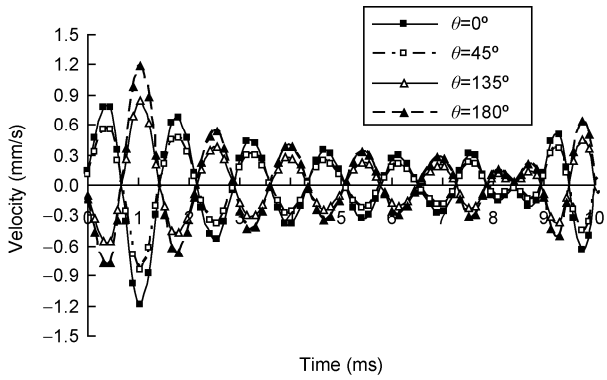

Figure 8 Comparison of velocity responses of mode v_{11} at different points.

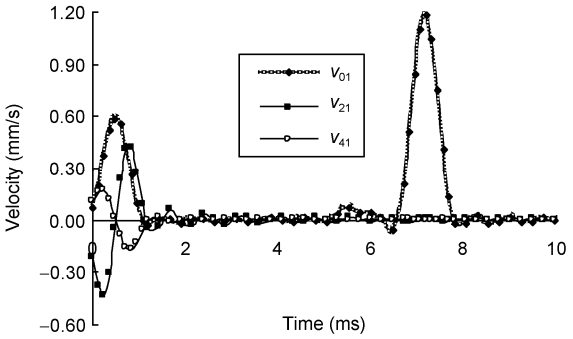

Figure 9 Comparison of velocity responses of modes of n=1 at 90° point.

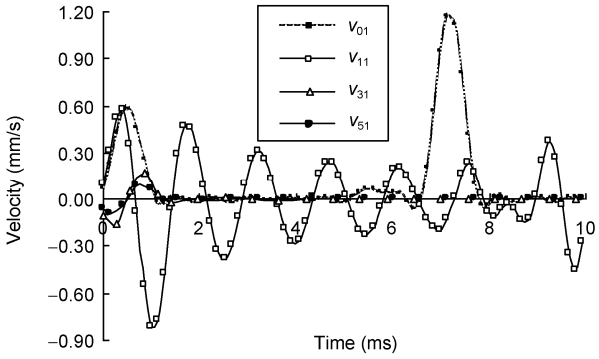

Figure 10 Comparison of velocity responses of modes of n=1 at 45° point.

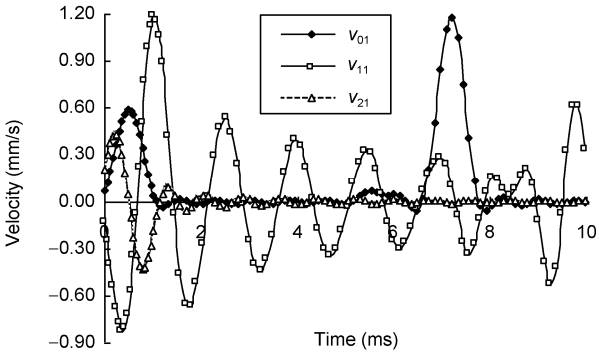

Figure 11 Comparison of velocity responses of modes of n=1 at 180º point.

with 0° or 180º is greater than 45° or 135°.

Because dominant frequency of high-frequency waves at 90° point comes from the second flexural mode (m=2), but it comes from the first flexural mode (m=1) at other locations, the interference frequency at 90° point is double of what at the other locations.

4 Frequency and influencing factors of high-frequency interference waves

The velocity response is disturbed by high-frequency waves, and frequency of the interference waves is related to the

position of measuring point, geometric properties of pile shaft, parameters of the material, etc. The velocity response spectrum at various points is shown in Figure 12. The interference frequency at 45°, 135° and 180° points is about 660–700 Hz, and that at 90° point is 1350 Hz, about two times of the former. Near the frequency 2050 Hz, there are other two high frequency interference wave crests, and the peak value at 90° point is the least. Table 3 presents the frequency of high-frequency interference waves with average radius R_0=0.34 m and 0.44 m. There are two main kinds of frequencies in low strain testing on PCC pile, the frequency at 90° point is about two times than the others.

Figures 13 and 14 show that the frequency of high-frequency interference varies with radius. It was found that the larger the radius, the smaller the frequency. When R_0=0.30, 0.34, 0.44 and 0.54 m, the frequencies are 1995, 1780, 1355 and 1095 Hz, respectively. The variety of frequency is nonlinear, and the slope of the curve tends to decrease with the increase of radius (as indicated in Figure 14).

Figure 15 shows comparison of velocity responses of pipe pile with different pile length at 90º point. The curves from 1.3 ms to 6.8 ms have little difference, which indicates that pile length has no effect on interference frequency. The new high frequency waves are excited when the reflected wave from bottom of the pile with H=10 m arrives at pile top at t=7.35 ms, so the curves from 7.8 ms to 13.6 ms are different from each other.

The interference frequency also depends on modulus of pile shaft. Comparison of frequency-domain velocity responses of pipe pile with different concrete modulus at 45° point is shown in Figure 16. As for the pile with E=15, 20, 25 and 30 GPa, the interference frequencies are 620, 700, 780 and 860 Hz, respectively. The interference frequency

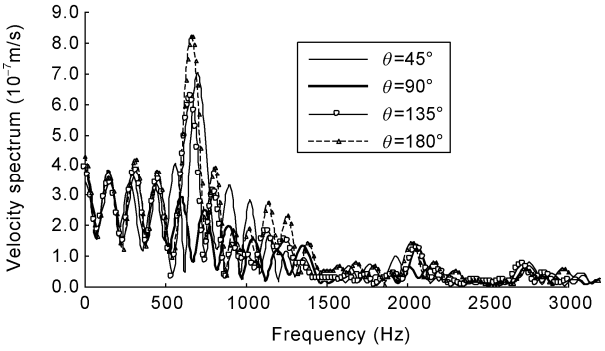

Figure 12 Comparison of frequency-domain responses at different points (z=0, r=0.44).

Table 3 Frequency of high-frequency interference wave at different points

Radius angle between exciting point and receiving points (°)	0	45	90	135	180
Frequency of interference waves for R_0=0.34 m (Hz)	880	880	1780	900	895
Frequency of interference waves for R_0=0.44 m (Hz)	690	700	1355	660	665

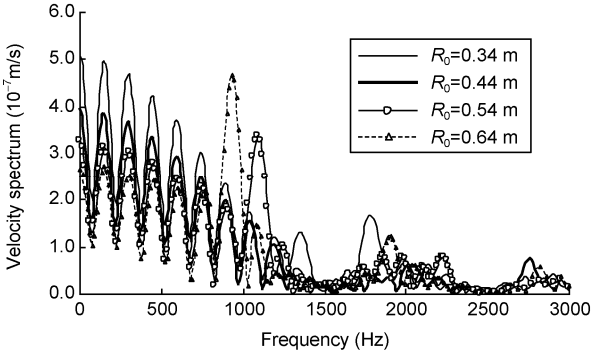

Figure 13 Comparison of frequency-domain velocity responses of pipe pile with different radius (z=0, θ=90, r=R_0).

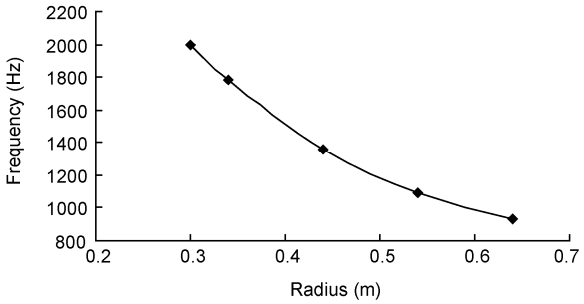

Figure 14 Effects of pile radius on frequency of high-frequency interference waves (z=0, θ=90, r=R_0).

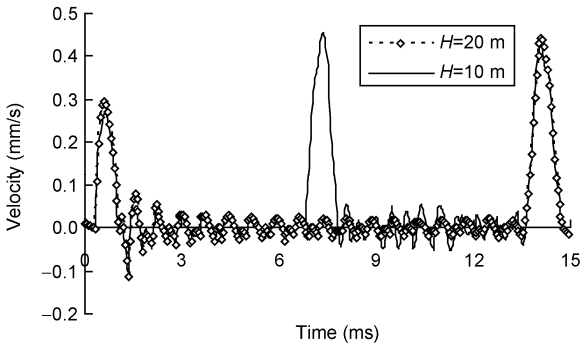

Figure 15 Comparison of velocity responses of pipe pile with different pile length (z=0, θ=90, r=0.44).

increases linearly as the increment of modulus (as shown in Figure 17).

The results indicate that the interference frequency is greatly influenced by geometry and mechanics characteristics of the pile such as radius and modulus.

5 Peak value and influencing factors of high-frequency interference waves

As shown in Figures 6 and 18, the peak value and phase of interference waves vary with the positions of receiving points. Figure 18 shows the effects of radius angle on peak value of high-frequency interference waves. At 0° (or 360°),

45° (or 315°), 135° (or 215°) and 180º points, the wave crests and hollows of interference waves emerge at the time t=1.71 ,2.43, 3.17 ms, etc. The peak value of which at 90° (or 270°) point is close to 0. The farther the distance away from 90° (or 270°) point, the larger the peak value of interference waves, as a result, the wave crests and hollows at 0° (or 360°) point and 180° point are maximal. The phases of interference waves from 0° to 90° (or 270° to 360°) are always contrary to those from 90° to 180° (or 180° to 270°) at any time t, so the phase difference is π. As the propagation of the waves, the peak values of interference waves gradually decrease, so the absolute values at time 5.35 ms and 6.07 ms are the least.

Figure 19 shows the velocity responses of pipe pile with different radius at 45° point. The figure shows that pile radius has little influence on peak value of interference waves but has great influence on peak value of the reflected waves. The impulse width has no effect on frequency but has great effect on peak value of interference waves (shown as Figure 20). Figure 21 shows effects of impulse width on peak value of high-frequency interference waves at 45° point. The figure indicates that the wider the impulse width, the smaller the peak value of high-frequency interference waves. The absolute value of slope increases as the increase of impulse width, so the wider impulse is more propitious to weaken high-frequency interference than narrower impulse. In application of low strain dynamic testing on PCC pile, wider impulse should be adopted to weaken peak value of high-frequency interference waves.

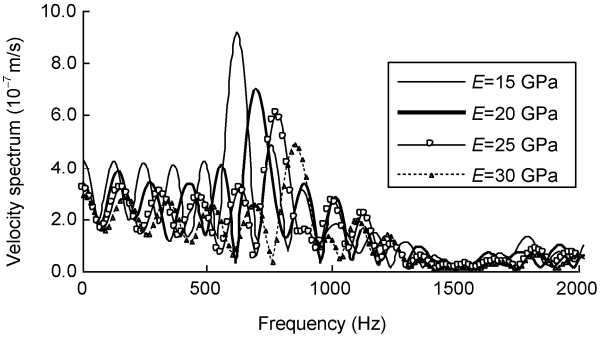

Figure 16 Comparison of frequency-domain velocity responses of pipe pile with different concrete modulus (z=0, θ=45, r=0.44).

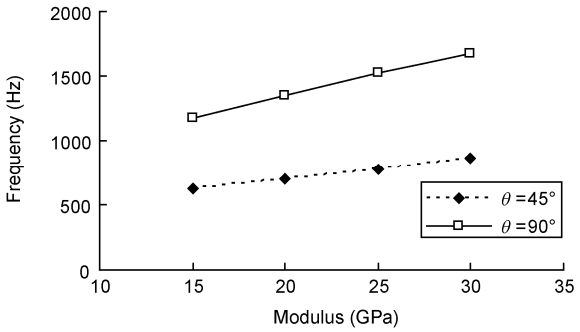

Figure 17 Effects of concrete modulus on frequency of high-frequency interference wave (z=0, θ=45, r=0.44).

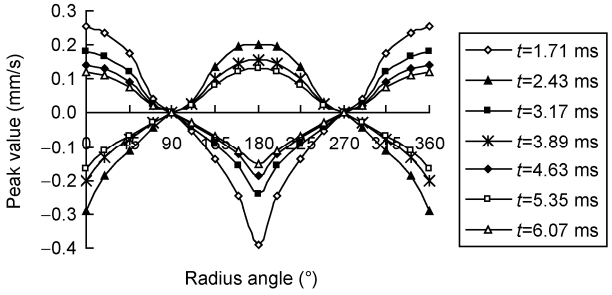

Figure 18 Effects of radius angle on peak value of high-frequency interference waves (z=0, r=0.44).

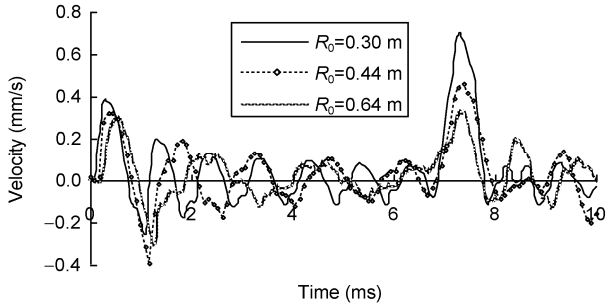

Figure 19 Velocity responses of pipe pile with different radius (z=0, θ=45, r=R_0).

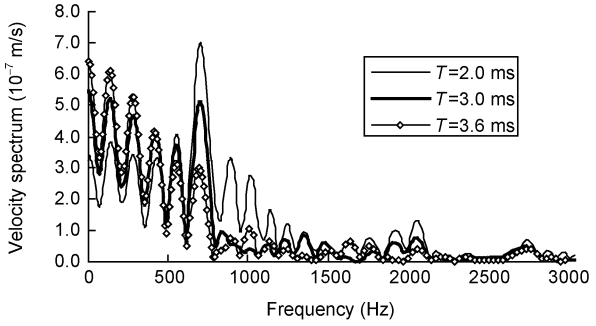

Figure 20 Frequency-domain velocity responses of pipe pile with different impulse width (z=0, θ=45, r=0.44).

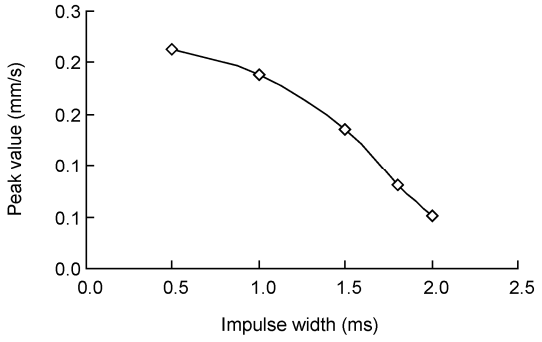

Figure 21 Effects of impulse width on peak value of high-frequency interference wave (z=0, θ=45, r=0.44).

frequency interference waves.

The peak values of high-frequency waves are influenced

by soil resistance. The soil coefficients are related to shear modulus and density [18], and the coefficients (per unit pile length) of soil around pile are proposed as

$$k = 2.75G_s, \tag{37}$$

$$\delta = 2\pi R\sqrt{\rho_s G_s}. \tag{38}$$

In this study, the coefficients per unit area on pile-soil interface are

$$k = 0.438G_s / R, \tag{39}$$

$$\delta = \sqrt{\rho_s G_s}, \tag{40}$$

where G_s is the shear modulus of the soil; ρ_s is the density.

The compression modulus E_s is commonly obtained by laboratory test, which can be transformed to shear modulus G_s by

$$G_s = \left(1 - \frac{2\nu_s^2}{1-\nu_s}\right)\frac{E_s}{2(1+\nu_s)}, \tag{41}$$

where ν_s is Poisson's ratio of the soil.

PCC piles are mainly used to reinforce soft soil, the compression modulus of which is about 2–5 MPa and the Poisson's ratio is about 0.25–0.4. The parameters of five cases are presented in Table 4.

With different soil parameters in Table 4, the elastic and damping coefficients can be calculated by eqs. (39)–(41). The velocity response is related to compression modulus and Poisson's ratio. Figure 23 reveals that as the decrease of Poisson's ratio, the peak values of interference waves are weakened. The curves in Figure 24 indicate that the increase of compression modulus also makes the peak values of interference waves to be weakened. The influence of soil parameters on high-frequency interference is unconspicuous at the 90° point (shown as Figure 24). The reflected waves are obviously reduced as the increase of compression modulus and decrease of Poisson's ratio (Figures 22–24).

Table 4 Calculation cases with different soil parameters

Calculation case	E_s (MPa)	ρ_s (g/cm^3)	ν_s
Case 1	2.00	1.80	0.40
Case 2	2.00	1.80	0.35
Case 3	2.00	1.80	0.30
Case 4	3.50	1.80	0.30
Case 5	5.00	1.80	0.30

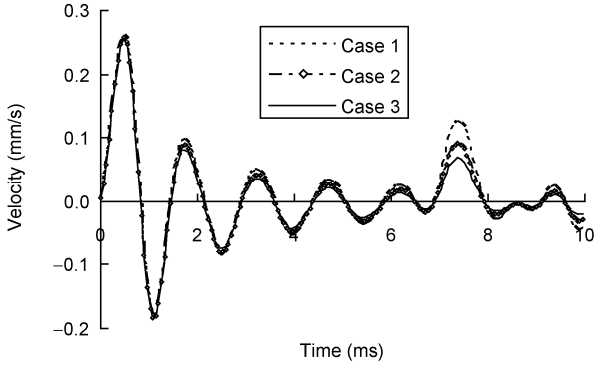

Figure 22 Time-domain velocity responses of pipe pile with different ν_s (z=0, θ=45, r=0.44).

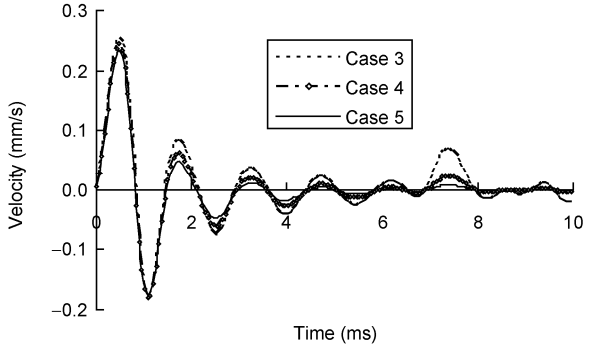

Figure 23 Time-domain velocity responses of pipe pile with different E_s (z=0, θ=45, r=0.44).

The peak values of cases 2, 3 and 4 are 3.07×10^{-7}, 2.83×10^{-7} and 2.23×10^{-7} m/s in frequency domain, respectively (Figure 25), however, the frequencies of interference waves of all the cases are near 700 Hz, which shows that soil resistance has great effect on peak value but has little effect on frequency of interference waves. As the propagation of stress wave, the weakening of peak value is more visible (Figures 22–24), so the peak value of high-frequency interference close to the reflected wave crests is very small and even invisible. The results indicate that the larger the soil resistance, the smaller the peak value of interference waves.

The results indicate that the peak value of high-frequency inference is related to external conditions such as impulse width and soil resistance, but independent of geometry and mechanics characteristics of the pile such as pile length, radius and modulus. Engineering practice indicates that a wider impulse will be excited if the hammer is softer or a hammer cushion is used, as a result, some external measures (soft hammer, hammer cushion) should be taken to weaken high-frequency interference, meanwhile, the point at the angle of 90° suffers the least high-frequency interference, thus the receiver should be close to this point.

6 Conclusions

An analytical solution of vertical vibratory response of large-diameter pipe piles in low strain testing was proposed in this paper. 1D wave theory, 3D FEM and model tests were employed to verify the validity of analytical solution. The high-frequency interference was investigated and the conclusions could be made as follows:

(1) The characteristic of high-frequency interference on pile top was analyzed. The peak values and phases of high-

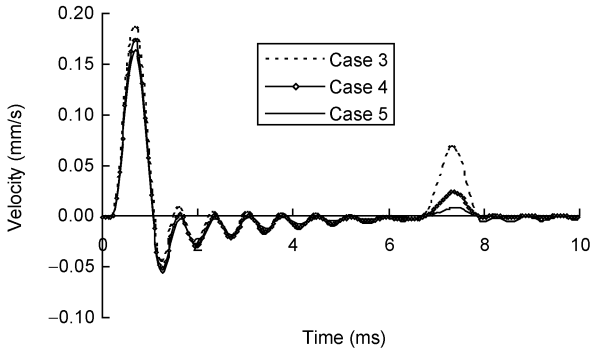

Figure 24 Time-domain velocity responses of pipe pile with different E_s (z=0, θ=90, r=0.44).

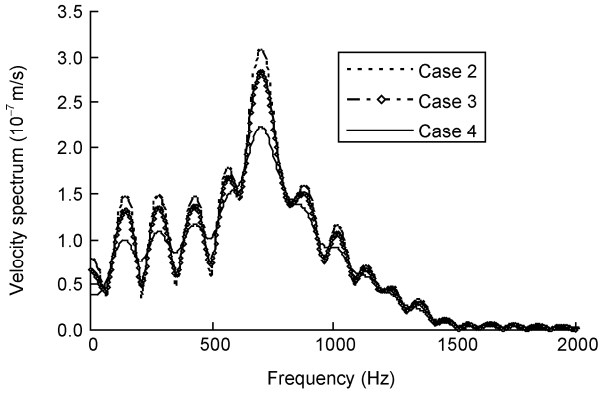

Figure 25 Frequency-domain velocity responses of pipe pile with different soil resistance (z=0, θ=45, r=0.44).

frequency interference waves are not the same at different points. The larger radius angle between the receiving and 90° points leads to greater peak value of high frequency wave crests. The point at the angle of 90° suffers the least high-frequency interference.

(2) The high-frequency interference at the angle of 90° mainly derives from the second flexural mode, but that at remaining angles mainly originates from the first flexural mode.

(3) The frequency of interference waves is influenced by the position of receiving point, pile radius and modulus, but independent of pile length, impulse width and soil resistance. The frequency increases with larger modulus of pile shaft and smaller pile radius.

(4) The peak value of high-frequency interference waves is influenced by the position of receiving point, impulse width and soil resistance, but independent of pile length, pile radius and modulus. The wider impulse width causes the smaller peak value. The interference waves are weakened as the increase of compression modulus and decrease of Poisson's ratio.

(5) The frequency of high-frequency interference waves is an intrinsic property of the pile and dependent on the geometric and mechanics properties of the piles, so the high-frequency interference waves cannot be eliminated but can be weakened. In engineering practice some appropriate external measures such as using soft hammer, hammer cushion and choosing optimal receiving point, should be taken to weaken peak value of high-frequency interference waves.

This work was supported by the National Natural Science Foundation of China (Grant No. 51008115) and the Provincial Science Foundation of Jiangsu (Grant No. BK2008040).

1 Liu H L, Fei K, Xu X T. Development and application of the large-diameter driven cast-in-place concrete thin-wall pipe pile. Proc of the 16th Int Conf on Soil Mech and Geotech Eng, Osaka, Japan, 2005. 2137–2140
2 Xu X T, Liu H L, Lehane B M. Pipe pile installation effects in soft clay. Geotech Eng, 2006, (GE4): 285–296
3 Liu H L, Charles W W Ng, Fei K. Performance of a geogrid-reinforced and pile-supported highway embankment over soft clay: case study. J Geotech & Geoen Eng, ASCE, 2007, 133(12): 1483–1493
4 Liu H L, Chu J, Deng A. Use of large-diameter, cast–in situ concrete pipe piles for embankment over soft clay. Can Geotech J, 2009, 46(8): 915–927
5 Likins G E, Rausche F. Recent advances and proper use of PDI low strain pile integrity testing. Sixth Int Conf on the Application of Stress-wave Theory to Piles, St.Paul, Brazil, 2000. 211–218
6 Massoudi N, Teffera W. Non-destructive testing of piles using the low strain integrity method. Proc of the Fifth Int Conf on Case Histories in Geotechnical Engineering, New York, 2004. 13–17
7 Smith E A L. Pile driving analysis by the wave equation. J Soil Mech & Found Div, ASCE, 1960, 86: 35–61
8 Rausche F. Soil response from dynamic analysis and measurement on piles. Ph.D. Dissertation. Div of Solid Mech, Structures and Mechanical Design, Case Western Reserve University, Cleveland Ohio, 1970
9 Rausche F. Soil resistance prediction from pile dynamics. J Soil Mech & Found Div, ASCE, 1972, 98(SM9): 917–937
10 Goble G G, Likins G E, Rausche F. Bearing capacity of piles from dynamic measurements. Final Report. Department of Civil Engineering, Case Western Reserve University, Cleveland, Ohio, 1975, 41–45
11 Goble G G, Hery P. Influence of residual forces on pile driveability. Second Int Conf of the Application of Stress-Wave Theory on Piles. Stockholm, 1984. 154–161
12 Rausche F, Goble G G, Likins G E. Investigation of dynamic soil resistance on piles using GRLWEAP. Proc of the Fourth Int Conf on the Application of Stress-Wave Theory to Piles, The Netherlands, 1992. 137–142
13 Morgano C M. Determining embedment depths of deep foundations using non-destructive methods. Fifth Int Conf on the Application of Stress-wave Theory to Piles, Orlando, FL, 1996. 734–747
14 Ding X M. Test study and analytic method research on vertical vibratory response of cast-in-situ concrete large-diameter pipe pile (in Chinese). Doctoral Dissertation. Nanjing: Hohai University, 2008
15 Chen F, Luo W Z. Dimension effect on low strain integrity testing of prestressed pipe piles (in Chinese). Chinese J Geotech Eng, 2004, 26(3): 353–356
16 Fei K, Liu H L, Zhang T. Three-dimensional effects in low strain integrity test of PCC pile (in Chinese). Rock & Soil Mech, 2007, 28 (6): 1095–1102
17 Liu H L, Tan H M. Development of large scale pile foundation model test system (in Chinese). Chinese J Geotech Eng, 2009, 31(3): 452–457
18 Lee S L, Chow Y K, Karunaratne G P, et al. Rational wave equation model for pile-driving analysis. J Geotech Eng, ASCE, 1988, 114(3): 306–325